Materials
Views
www.MaterialsViews.com

ADVANCED
FUNCTIONAL
MATERIALS
www.afm-journal.de

FULL PAPER

Design and Synthesis of "All-in-One" Multifunctional FeS₂ Nanoparticles for Magnetic Resonance and Near-Infrared Imaging Guided Photothermal Therapy of Tumors

Zhouqi Meng, Fang Wei, Wujun Ma, Nuo Yu, Peiling Wei, Zhaojie Wang, Yueqin Tang, Zhigang Chen,* Huiping Wang,* and Meifang Zhu*

The ideal theranostic nanoplatform for tumors is a single nanoparticle that has a single semiconductor or metal component and contains all multimodel imaging and therapy abilities. The design and preparation of such a nanoparticle remains a serious challenge. Here, with FeS₂ as a model of a semiconductor, the tuning of vacancy concentrations for obtaining "all-in-one" type FeS₂ nanoparticles is reported. FeS₂ nanoparticles with size of ≈30 nm have decreased photoabsorption intensity from the visible to near-infrared (NIR) region, due to a low S vacancy concentration. By tuning their shape/size and then enhancing the S vacancy concentration, the photoabsorption intensity of FeS₂ nanoparticles with size of ≈350 nm (FeS₂-350) goes up with the increase of the wavelength from 550 to 950 nm, conferring the high NIR photothermal effect for thermal imaging. Furthermore, this nanoparticle has excellent magnetic properties for T_2-weighted magnetic resonance imaging (MRI). Subsequently, FeS₂-350 phosphate buffer saline (PBS) dispersion is injected into the tumor-bearing mice. Under the irradiation of 915-nm laser, the tumor can be ablated and the metastasis lesions in liver suffer significant inhibition. Therefore, FeS₂-350 has great potential to be used as novel "all-in-one" multifunctional theranostic nanoagents for MRI and NIR dual-modal imaging guided NIR-photothermal ablation therapy (PAT) of tumors.

1. Introduction

Nanotechnology holds the promise of developing novel and more effective nanomaterials for the diagnosis and/or therapy of tumors that pose serious threat to human health.[1] To detect the tumor, many kinds of nanomaterials have been developed for the imaging of tumor, such as magnetic (Fe[2]/Gd[3]/Mn[4]-based) nanoparticles for magnetic resonance imaging (MRI), luminescent (such as lanthanide[5]/carbon[6]-based) nanoparticles for fluorescent imaging, and high atomic number or high X-ray attenuation coefficient nanomaterials (iodine[7]/gold[8]/bismuth[9]-based) for X-ray computed tomography (CT) imaging. Furthermore, to cure the tumor, various nanomaterials have also been investigated for developing new therapy methods, including nanocarriers (mesoporous silica,[10] polymer nanocapsules[11]) for advanced chemotherapy, nanophotosensitizers[12] for the photodynamic therapy and photothermal nanoagents for the ablation of tumor. Among these therapy methods, near-infrared (NIR) laser-induced photothermal ablation therapy (PAT) has drawn much attention as a minimally-invasive and potentially more effective technology.[12b,13] For achieving the NIR-PAT for tumors, several types of photothermal nanoagents have been well researched, containing polymer[14]/metal[15]/carbon[6]/semiconductor[16]-based nanomaterials. Our group has also prepared Cu[16a,17]/W[16b,18]-based semiconductors as novel and efficient photothermal agents. To further enhance the therapy efficiency and minimize side effects from NIR-PAT, the combination of NIR-PAT with bioimaging has been proposed for the simultaneous diagnosis and therapy of tumors, since bioimaging in vivo can be used to guide the design of NIR-PAT plans, for example, by choosing the optical doses and/or optimal irradiation region, and deciding the best timing of laser treatment when the photothermal agent reaches the peaked accumulation in the targeted lesion.[19]

For realizing the imaging-guided NIR-PAT, multifunctional nanomaterials, which contain NIR photothermal conversion ability and at least one of bioimaging functions, should be designed and prepared. Currently, three kinds of multifunctional nanomaterials with complex structures have been chiefly developed. The first kind is the mixture containing two or more imaging/therapy agents that are encapsulated/conjugated by organic/polymer molecules, including metal–metal,[3,20]

Dr. Z. Q. Meng, Dr. W. J. Ma, Dr. N. Yu, Dr. P. L. Wei,
Dr. Z. J. Wang, Prof. Z. G. Chen, Prof. M. F. Zhu
State Key Laboratory for Modification of Chemical
Fibers and Polymer Materials
College of Materials Science and Engineering
Donghua University
Shanghai 201620, China
E-mail: zgchen@dhu.edu.cn; zmf@dhu.edu.cn
Prof. F. Wei, Y. Q. Tang, Prof. H. P. Wang
Experimental Research Center
The First People's Hospital
Shanghai Jiaotong University
Shanghai 201620, China
E-mail: tywhp9618@msn.com

FULL PAPER

metal–polymer,[3,21] polymer–polymer[4a,14] or metal–carbon based blending material.[22] They can simultaneously deliver the multiple of diagnostic and therapeutic functions for tumor, enabling the well detection and treatment effects in a single procedure. The second type is Janus nanoparticles, such as metal-based alloy,[23] Au-based,[24] or metal-Se based janus,[25] whose functions can be well tuned. The last kind is core-shell nanoparticles, including metal@metal/polymer,[2a,26] metal@silical/polystyrene–metal/polymer,[27] as the core@shell structure. Our group has developed $Fe_3O_4@Cu_{2-x}S$ nanoparticles for MRI-thermal dual-modal imaging and NIR-PAT of tumor.[26b] However, these multifunctional nanomaterials suffer from some limitations, such as complex compositions, difficult fabrication, unsatisfactory imaging or therapeutic performances.

Ideally, one nanoparticle with single semiconductor or metal component should have all functions including multimodel imaging and NIR photothermal abilities. Thus, the design and preparation of "all-in-one" type of multifunctional nanoparticle with single component have attracted much attention. Recently, W-based (WS_2,[28] Rb_xWO_3[29]) or Cu_3BiS_3[30] single nanoparticle has been found to exhibit both CT-imaging and NIR-PAT abilities, since W and Bi are heavy elements with strong X-ray attenuation ability; and the correspondingly nanomaterials have strong NIR photoabsorption. But there are few reports on single nanoparticle that contains simultaneously bioimaging (beyond CT/photoacoustic imaging) and NIR photothermal performances. Thus, it is a major challenge to explore new "all-in-one" type nanoparticle with single component through facile controllable fabrication methods for the imaging guided NIR-PAT of tumors.

Iron (Fe) is an essential element for human beings, and it is of course more biocompatible than the above heavy elements (W, Bi). Fe-based semiconductors have the tuned magnetic properties for MRI and NIR-PAT of tumors, such as $FeSe_2$[31]

and FeS[32] nanomaterials. But these Fe-based semiconductors have the decreased NIR photoabsorption with the increase of wavelength and thus unsatisfactory NIR photothermal performances.[31,32] Usually, in the synthesis of Fe-based semiconductors, only equivalent-valency ions are normally incorporated, leading to no or low ionized free carriers. However, high concentration of free carriers is the prerequisite for achieving effective localized surface plasmon resonances (LSPRs) and then the intense NIR photoabsorption band.[33] Fortunately, carrier concentrations of semiconductors can be tuned by doping and/or promoted by defect structure.[33,34] With FeS_2 as a model of p-type Fe-based semiconductor, in the present work we reported the controllable synthesis of PEGylated FeS_2 nanoparticles with high carrier concentrations by a one-step solvothermal route. PEGylated FeS_2 nanoparticles with diameter of >300 nm (e.g., FeS_2-350) exhibit strong NIR photoabsorption band due to LSPRs, which is significantly different with FeS_2 nanocrystals with size of about <50 nm (e.g., FeS_2-30) and no NIR photoabsorption band.[35] FeS_2-350 can be served as the excellent photothermal agents for the simultaneous NIR imaging and NIR-PAT of in vivo tumor cells. Furthermore, they remained excellent magnetic property for T_2-weighted MRI, which can be used as the MRI contrast agents for tumors in vivo, leading to the guide of the therapies. More importantly, these PEGylated FeS_2-350 nanoparicles (NPs) can be excreted from the mice body.

2. Results and Discussion

2.1. Synthesis and Characterization of FeS₂

The crystal form of pyrite FeS_2 is typically NaCl-like cubic structure (**Figure 1**a). All Fe ions are octahedral coordinated by six S ions at equal distances, and each S ion has three Fe neighbors
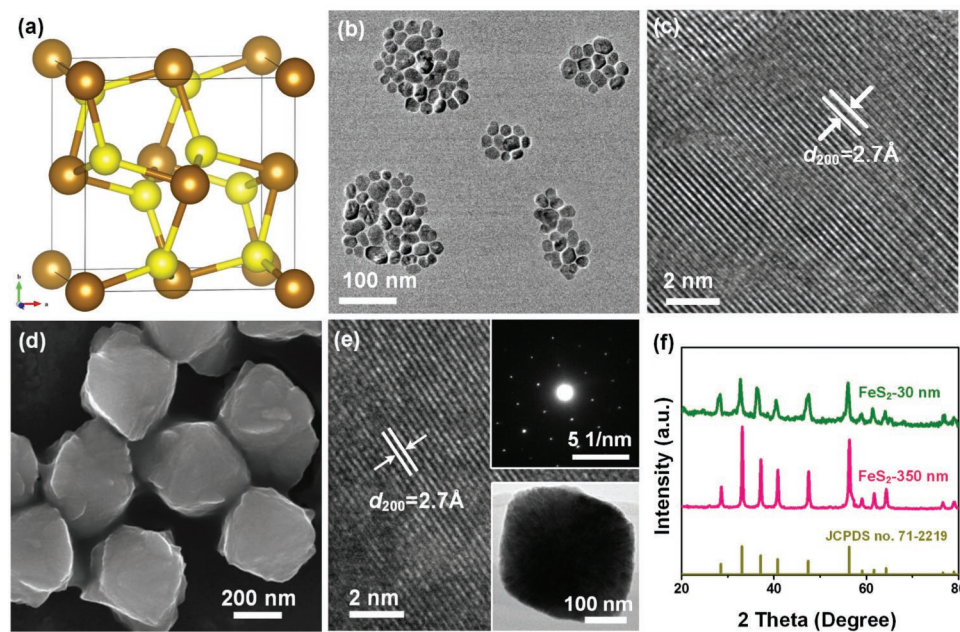
Figure 1. a) The crystal structure of pyrite FeS_2. b,c) TEM images of FeS_2 nanocrystals with small diameter of ≈30 nm (FeS_2-30). d,e) SEM and TEM images of FeS_2 with big diameter of ≈350 nm (FeS_2-350). Inset showing the TEM image and SAED patterns. f) XRD patterns.
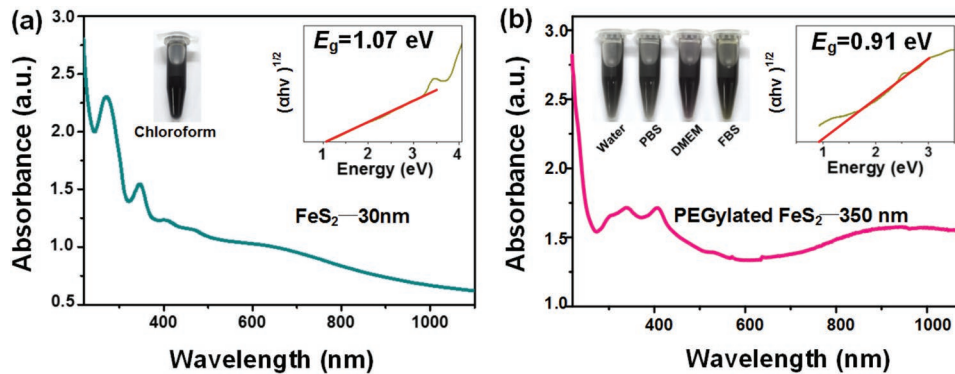
Figure 2. UV–vis-NIR spectra of a) FeS_2-30 solution and b) FeS_2-350 solution (2 mg mL^{-1}). The insets shows the determination of band gap and/or the photos of FeS_2-30 in chloroform and FeS_2-350 in different solvent (water, PBS, DMEM, FBS) after stored for two weeks.

and one S neighbor.[36] Pyrite FeS_2 nanoparticles (NPs) with small size (<50 nm) have been well developed for constructing solar photovoltaic and photoelectrochemical cells,[37] but they exhibit the decreased photoabsorption with the increase of wavelength from ≈500–1100 nm, due to the absence of efficient LSPR resulting from low free carrier densities. Fortunately, it has been found that free carrier densities and LSPR of semiconductors can be tuned by their composition, shape, phase, and size.[35a,38] To tune LSPR and then obtain intense NIR photoabsorption band, in the present work, we prepared two kinds of FeS_2 NPs with different size and shapes by two modified synthesis methods, containing pyrolysis[37,39] and solvothermal route.[38b,40]

When FeS_2 sample was prepared by a modified pyrolysis method,[37] they consists of colloidal nanocrystals with diameters of ≈30 nm (abbreviated as FeS_2-30) as shown in the transmission electron microscopy (TEM) image (Figure 1b). HR-TEM image (Figure 1c) shows an interplanar spacing of 2.70 Å, which corresponds to the *d*-spacing of the (200) planes of pyrite FeS_2 crystal. Moreover, when FeS_2 sample was prepared by the modified solvothermal route with the ethylene glycol as the solvent and polyethylene glycol (PEG)/polyvinyl pyrrolidone (PVP) as the surfactant,[38b] it is composed of uniform octahedral-shape with an average diameter of 357 ± 20 nm (abbreviated as FeS_2-350 NPs), as demonstrated in field emission scanning electron microscopy (SEM) and TEM images (Figure 1d and the inset in Figure 1e). The size distribution

(357 ± 20 nm) is consistent with the hydrodynamic diameter of 355 nm (Figure S1, Supporting Information). Meanwhile, from the HR-TEM image (Figure 1e), the lattice fringes can be clearly observed, and the interplanar *d*-spacing is measured to be 2.7 Å, corresponding to the (200) crystal planes. In addition, the selected area electron diffraction (SAED) pattern shows regular spots (Figure 1e inset), suggesting the single crystal of the nanoparticle. To further investigate their phase, both FeS_2 samples were evaluated by X-ray diffraction (XRD) pattern (Figure 1f). Both samples exhibit strong and well-defined diffraction peaks which can be well indexed to the pyrite (JCPDS no. 71-2219). And no impurity peak can be found in these samples. These results verify the well formation of FeS_2-30 and FeS_2-350 with pyrite structure.

We further investigated the photoabsorption properties of both FeS_2-30 and FeS_2-350. FeS_2-30 can be well dispersed in chloroform due to the presence of octadecylamine ligands, while FeS_2-350 can be well dispersed in water or growth medium (such as PBS, Dulbecco's modified Eagle medium (DMEM), fetal bovine serum (FBS)) due to the presence of biological ligands of PEG-400 ligands (confirmed by FTIR, Figure S3, Supporting Information). The optical properties of FeS_2-30 chloroform dispersion and FeS_2-350 aqueous dispersion were respectively measured by UV–vis-NIR spectroscopy (**Figure 2**). Obviously, the photoabsorption intensity of FeS_2-30 goes down with the increase of wavelength from 380 to 1100 nm (Figure 2a), yielding relatively large band-gap of 1.07 eV and low
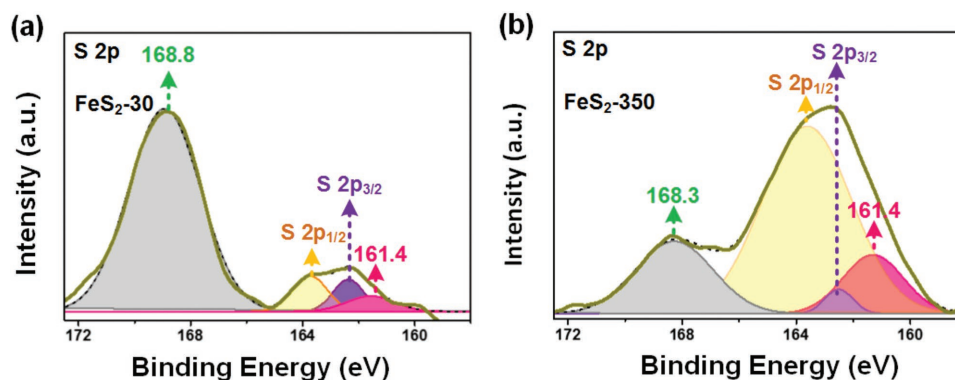

Figure 3. S 2p region XPS spectra of a) FeS_2-30 and b) FeS_2-350.

NIR photoabsorption. This spectrum is similar to the previous reports for the typical pyrite FeS_2.[37] Furthermore, FeS_2-350 has a short-wavelength absorption edge at ≈570 nm, reaching a minimum around 610 nm. The bandgap of FeS_2-350 can be determined to be ≈0.91 eV, which is significantly lower than that (1.07 eV) of FeS_2-30. Importantly, FeS_2-350 exhibits the enhanced photoabsorption intensity with the increase of wavelength from 550 to 1100 nm and reaches the maximum at 950 nm (Figure 2b). This intense NIR photoabsorption band is very similar to that of the typical semiconductor photothermal nanoagents ($W_{18}O_{49}$ nanowires with oxygen-deficiency[16b] and $Cu_{2-x}S$ with Cu-deficiency[17]), which have appreciable deficiency concentration.

To investigate the deficiency type and concentrations of FeS_2-350, the stoichiometry and the chemical state of its constituent elements were measured by the energy-dispersive X-ray spectroscopy (EDS) pattern and X-ray spectroscopy (XPS) analysis (Figure S2, Supporting Information). For comparison, the stoichiometry of FeS_2-30 was also studied. EDS pattern and XPS spectra demonstrate that there are Fe and S elements in both FeS_2-30 and FeS_2-350 samples, besides C or O elements from surface ligands (such as PEG-400 or octadecylamine). For FeS_2-30 sample, the ratio of S to Fe is determined to be 1.99 which is very close to the ideal stoichiometry (S/Fe = 2). Interestingly, FeS_2-350 exhibits an obviously low S/Fe ratio (1.84), suggesting the presence of high S vacancy. It has been revealed that the pyrite FeS_2 has Fe-vacancy (V_{Fe}) and S-vacancy (V_S).[41] Usually, when S element is poor (such as S/Fe < 1.9), [Vs] tends to become the main deficiency in pyrite.[41b,42] With the decrease of S/Fe ratio, the S vacancy concentrations in pyrite goes up, even reaching as high as 7.5% when S/Fe ratio is 1.75.[41a]

To further illustrate the presence of high S vacancy, in the present work, we performed S 2p XPS analysis for PEGylated FeS_2-350. For comparison, S 2p XPS spectrum of FeS_2-30 was also analyzed. **Figure 3** shows the typical S 2p spectra of FeS_2-30 and FeS_2-350. For FeS_2-30 sample, there is a strong peak at 168.8 eV (area: 83.2%) which can be attributed to SO_4^{2-} on the surface (169.5–167.5 eV),[38b,43] illustrating the serious surface oxidization from FeS_2 to ferric sulfates, similarly with previous researches.[39] On the contrary, the peak at 168.3 eV for FeS_2-350
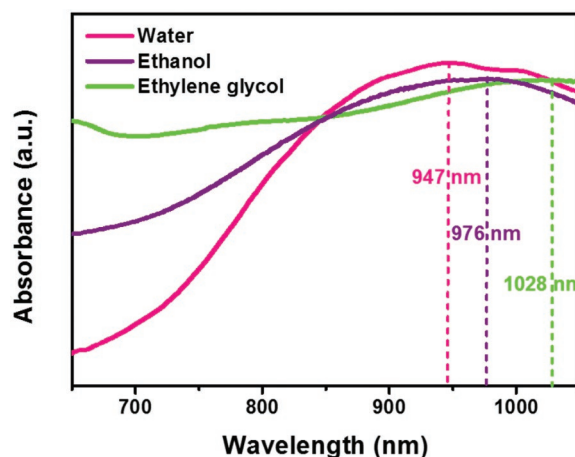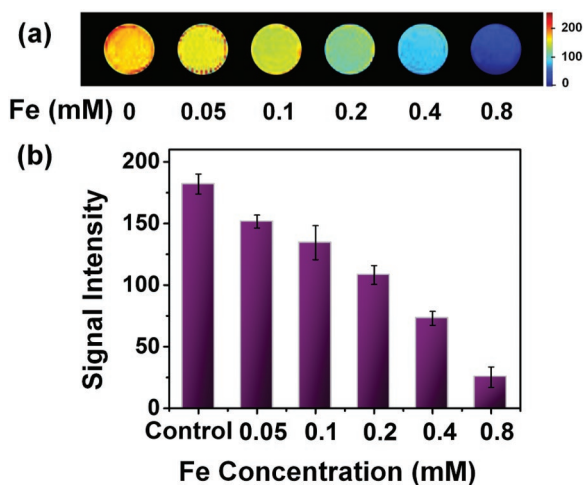

Figure 4. The NIR absorbance of PEGylated FeS_2-350 dispersed in varying solvents with increasing refractive index. The refractive indexes of water, ethanol, and ethylene glycol are 1.333, 1.367, and 1.430, respectively.

is relatively low (peak area: 21.2%), indicating the slight surface oxidization. Furthermore, S 2p spectra for FeS_2 can be fitted by three nearly Gaussian, centered at 163.7, 162.5, and 161.4 eV. The binding energy at 163.7 and 162.5 eV can be respectively assigned to S $2p_{1/2}$ and $2p_{3/2}$ of surface sulfur S_2^{2-} dimers from pyrite FeS_2.[43,44] Furthermore, the binding energy at 161.40 eV is directly related to the monovacancy species S^{2-} at the surface.[41b] The peak at 161.40 eV for FeS_2-30 sample is low (4.2%), while the peak at 161.40 eV for FeS_2-350 sample is strong (13.4%). Based on these facts, one can deduce that FeS_2-30 sample may have serious surface oxidization and lower S vacancy, while FeS_2-350 sample has the weak surface oxidization and very high S vacancy. High S vacancy from FeS_2-350 sample may confer high concentration of free carriers, which facilitate to produce strong LSPRs for FeS_2-350.[33]

It is well known that one of LSPR features is the absorption band redshifts with increasing solvent refractive index.[30,35a] To further confirm LSPR of FeS_2-350, we also detected the NIR absorption of PEGylated FeS_2-350 in solvents with differing refractive indexes (**Figure 4**). Obviously, with the increase of refractive indexes from 1.333 (water) to 1.367 (ethanol) and
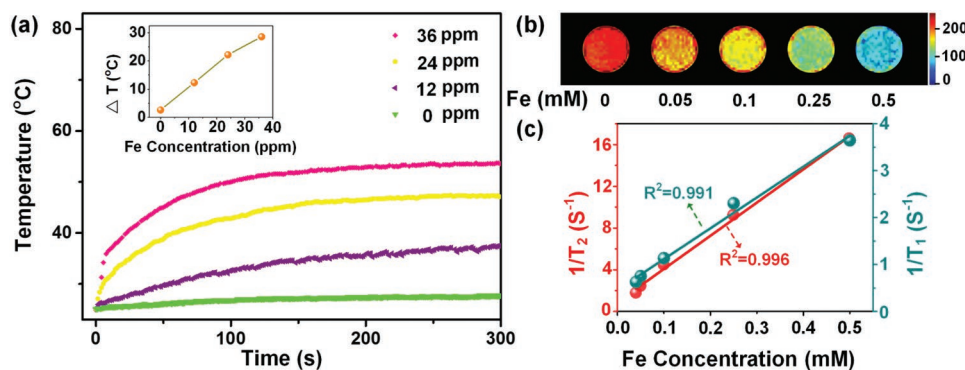
Figure 5. Photothermal performance and magnetization properties. a) Temperature profiles of pure water and aqueous dispersions of PEGylated FeS_2-350 at different concentrations determined by the Fe content as a function of irradiation time. Insert showing the plot of temperature elevation (ΔT) over 300 s versus Fe concentration. b) Color-coded T_2-weighted MRI photographs of the dispersions with different Fe concentrations at room-temperature. c) The corresponding T_1 and T_2 relaxation rate ($1/T_1$ or $1/T_2$) of the dispersions as a function of Fe concentration.

Materials
Views
www.MaterialsViews.com

ADVANCED
FUNCTIONAL
MATERIALS
www.afm-journal.de

FULL PAPER

Figure 6. T_2-weighted MRI in vitro. a) T_2-weighted MRI images and b) signal intensity analysis of 7721 cells after treated with PEGylated FeS$_2$-350 with various Fe concentration. The data are shown as mean ± standard deviation (SD).

1.430 (ethylene glycol), the maximum absorption wavelength shifts from 947 to 976 nm and 1028 nm, indicating a continuous red-shift. The red-shift phenomenon of FeS$_2$-350 is similar to the previous reports on LSPRs,[30] and it also supports the presence of strong LSPR which results in intense NIR photoabsorption in anion-deficient semiconductor.[45]

2.2. "All-In-One" MRI and Photothermal Performance

Strong NIR photo-absorption of PEGylated FeS$_2$-350 may confer high NIR-photothermal conversion performance. To analyze the photothermal performance, the aqueous dispersions containing FeS$_2$-350 with various Fe concentrations (0–36 ppm) were respectively irradiated by 915-nm laser with intensity of 1.0 W cm^{-2}, and their temperature were recorded (**Figure 5**a). The blank test reveals that the pure water (without PEGylated FeS$_2$-350) exhibits a low temperature elevation of less than 3 °C from the room temperature (25 °C). Interestingly, when FeS$_2$-350 with Fe concentrations (12, 24, 36 ppm)
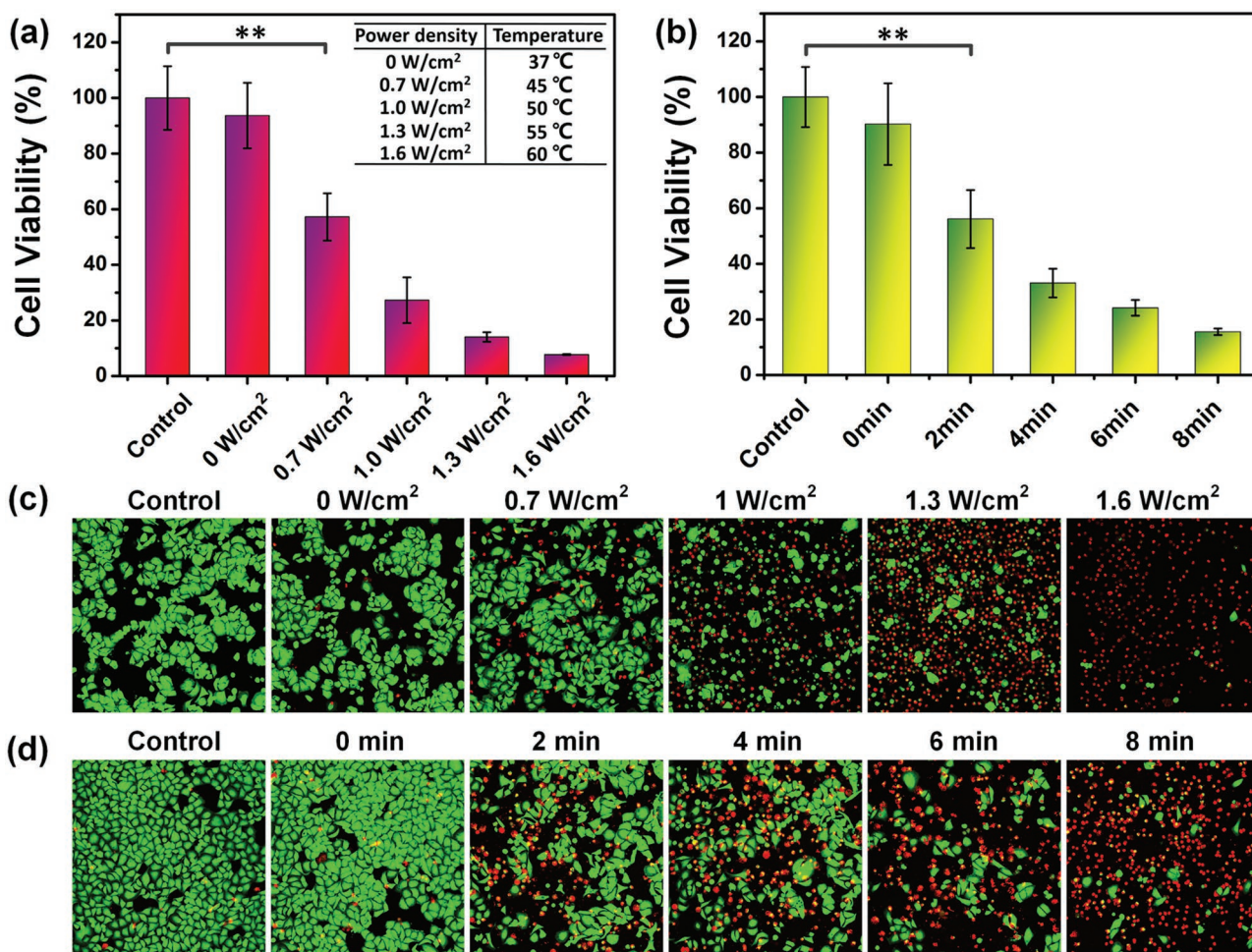
Figure 7. In vitro controllable photothermal treatment driven by 915-nm laser. a) Relative viabilities of 7721 cell incubated with PEGylated FeS$_2$-350 with different laser intensity (0–1.6 W cm^{-2}) for 5 min, and b) with 1.0 W cm^{-2} (maintained 50 °C) for various irradiation time (0–8 min). The data are shown as mean ± SD. Error bars are based on at least triplicate measurements. *$P < 0.05$, **$P < 0.01$. c,d) The confocal images of 7721 cells after stained by calcein-AM and ethidium homodimer-1 at different post-treatment, viable or dead cell were stained green by calcein-AM or red by ethidium homodimer-1 respectively.

is dispersed in water, the temperatures of the aqueous dispersions go up rapidly under the irradiation of 915-nm laser from 0 to ≈100 s, then exhibit relatively slow heating-rate from 100 to 200 s, and reach the maximum at 250–300 s. The heating rate became slower at higher temperature due to faster heat-loss.[16b] In addition, the temperature elevation (ΔT) at 300 s, which is calculated from Figure 5a, ascends almost linearly from ≈2.61 to 28.6 °C with the increase of the Fe concentration from 0 to 18 ppm (the inset in Figure 5a). The photothermal conversion efficiency of FeS$_2$-350 is determined to be 33.1% (Figure S4, Supporting Information) which is higher than that (25.7%) of Cu$_9$S$_5$ nanocrystals developed by our group.[17] Moreover, FeS$_2$-350 nanoparticles show excellent photothermal stability after five cyclically laser ON/OFF irradiation (Figure S5, Supporting Information). All these facts reveal that FeS$_2$-350 has efficient and stable photothermal effects.

Usually, Fe-based nanomaterials have the magnetic properties for MRI.[32,46] To verify MRI ability, aqueous dispersions of PEGylated FeS$_2$-350 with different Fe concentration (0–0.5 × 10^{-3} M) were examined by using T_2-weighted MRI on a 0.5 T scanner (Figure 5b,c), and the transverse relativity (r^2, the transverse relaxation rate per millimolar of iron) was calculated (Figure 5b,c). The MRI images are colored to get the remarkable visualization of the contrast changes. Obviously, the T_2 signal intensity gradually decreases with the increase of Fe concentration, revealing the concentration-dependent coloring effect (Figure 5b). Furthermore, by plotting the corresponding transverse relaxation ($1/T_2$) as a function of the Fe concentration (Figure 5c), the r_2 of PEGylated FeS$_2$-350 is calculated to be 31.836× (10^{-3} M)$^{-1}$s^{-1}. In addition, the r_1 is determined to be 6.566 × (10^{-3} M)$^{-1}$s^{-1}, and the r_2/r_1 ratio (4.8) is higher than 3, which enable PEGylated FeS$_2$-350 to be a negative contrast enhancement.[47] These facts verify strong magnetic properties of FeS$_2$-350 for T_2-weighted in MRI.

Based on the above results, one can conclude that FeS$_2$-350 is "all-in-one" type multifunctional nanoparticle with MRI ability and NIR photothermal effect, resulting in the promising potential in MRI and NIR imaging guided NIR-PAT for tumor.

2.3. T_2-Weighted MRI and Photothermal Therapy In Vitro

Subsequently, we examined the feasibility of FeS$_2$-350 in the MRI in vitro. Humans hepatocarcinoma cells SMMC-7721 (7721 cells) were treated with various concentrations of PEGylated FeS$_2$-350 (Fe concentration 0–0.8 × 10^{-3} M), and then the T_2-weighted MRI scanning were performed. Colorful images are allowed to easily visualize the contrast changes. Significantly, compared to the control, an increasing deep colored images are observed with the increase of Fe concentration in T_2-weighted MRI images (**Figure 6**a), which suggests that the particles can reduce the signal intensity rapidly. Furthermore, the signal intensity from T_2-weighted MRI images goes down with the increase of Fe concentration (Figure 6b), in agreement well with T_2-weighted MR imaging results (Figure 6a). These results demonstrate that FeS$_2$-350 can be served as an effective contrast agents for T_2-weighted MR imaging of cancer cells.

Ideal nanomaterials should be nontoxic for biomedical applications, and thus the potential cytotoxicity of FeS$_2$-350 was
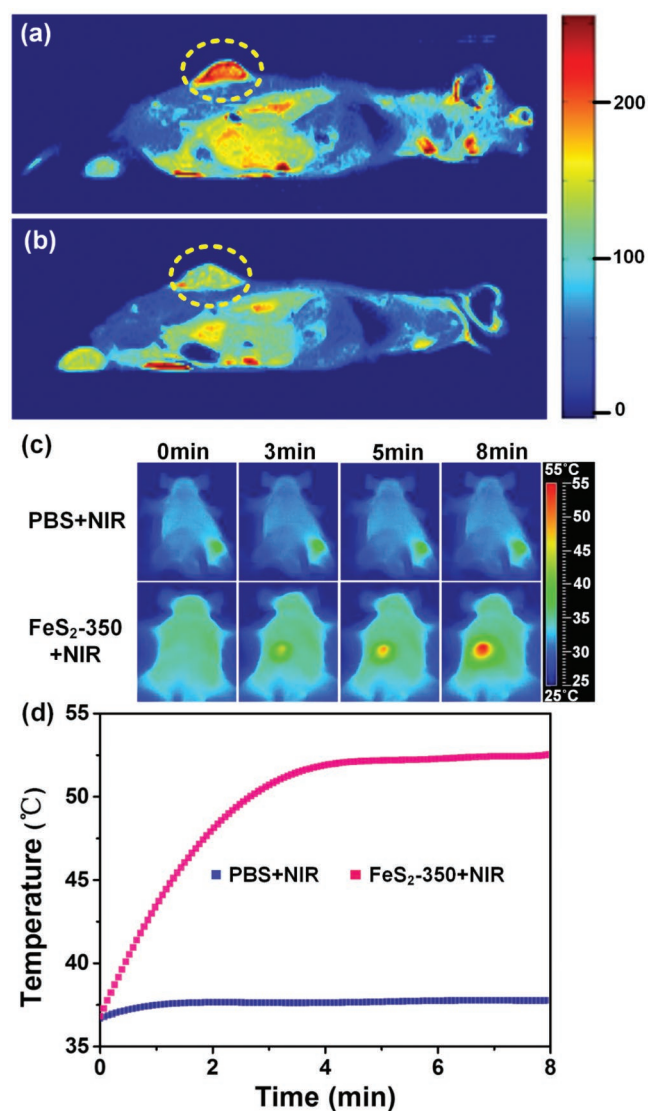
Figure 8. MRI and NIR images for animal. a,b) In vivo MRI images of tumor before and after intratumorally injected with PBS solution of PEGylated FeS$_2$-350 (1 mg mL^{-1}), respectively. c) Infrared thermal image for tumor-bearing mice exposed to the NIR laser (915-nm, 1.0 W cm^{-2}) at post-injection of PBS or PEGylated FeS$_2$-350 (500 µg mL^{-1}). d) The tumor temperatures of mice from (c) monitored by the IR thermal camera during laser irradiation. Color bar on right shows temperature in degrees celcius.

investigated by using 7721 cells. 7721 cells were incubated in FeS$_2$-350 dispersion with various concentrations for 24 h. Then the standard cell counting kit-8 (CCK-8) assay was carried out to evaluate the relative viabilities of 7721 cells. It can be seen that a high cells viabilities can be obtained (>90%) even at high concentrations (reaching to 1000 µg mL^{-1}) of FeS$_2$-350 (Figure S6, Supporting Information), suggesting a very low cytotoxicity and promising application in biomedicine.

Next, the photothermal therapeutic effects of FeS$_2$-350 in vitro was studied. 7721 cells were treated with PEGylated FeS$_2$-350 in the presence of 915-nm laser irradiation with different intensity (0–1.6 W cm^{-2}, insert table in **Figure 7**a) for 5 min (Figure 7a). Obviously, without the irradiation of NIR laser (0 W cm^{-2}), cell

www.MaterialsViews.com

ADVANCED
FUNCTIONAL
MATERIALS
www.afm-journal.de

FULL PAPER
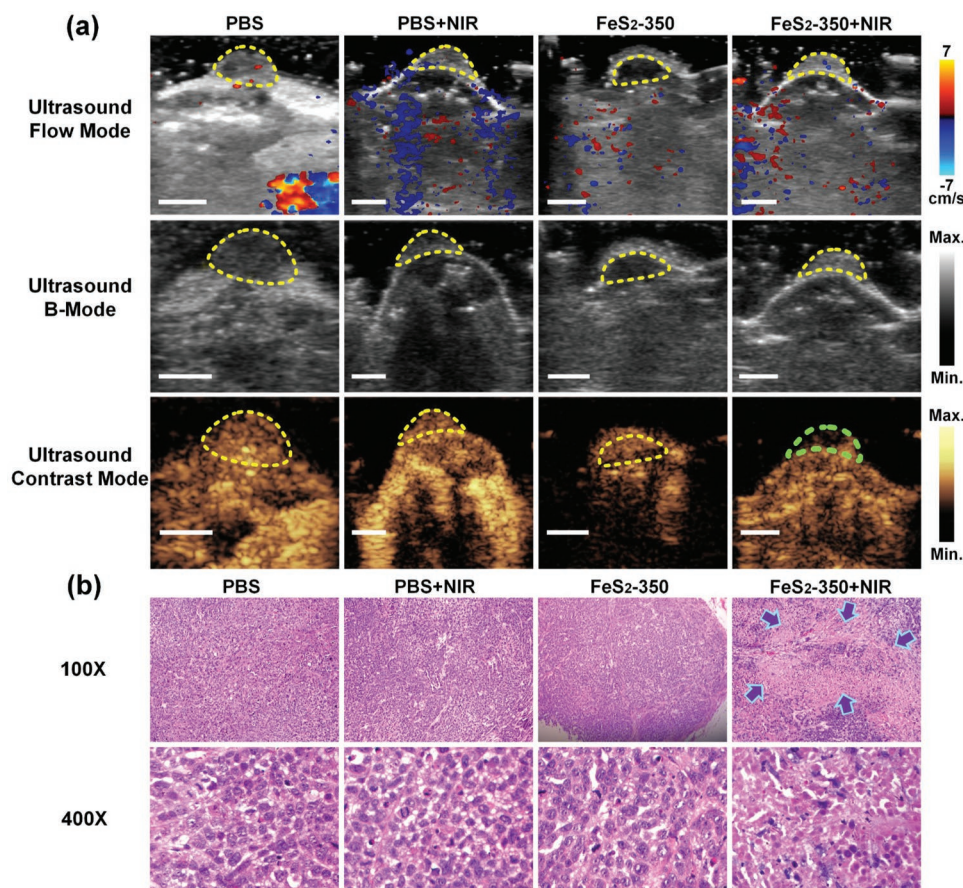
Figure 9. In vivo immediate effects. a) In vivo ultrasound image of flow mode (upper row), B-mode (middle row) and contrast mode (lower row) for tumor bearing mice after different treatments by the NIR laser (915-nm, 1.0 W cm^{-2}, 10 min). Scale bar: 5 mm. b) H&E stained tumor sections collected from different group mice at post-treatments. The magnifications are 100× (upper row) and 400× (lower row).

viability remains high level (>90%), illustrating low cytotoxicity. On the contrary, with the laser intensity increasing from 0 to 1.6 W cm^{-2}, the temperature of aqueous FeS$_2$-350 dispersion goes up from 37 to 60 °C (the inset in Figure 7a), resulting in the significant decrease of cell viability (Figure 7a). Specifically, when the laser intensity is or exceeds 0.7 W cm^{-2}, cell viabilities show a remarkable reductions (such as $P < 0.01$ for 0.7 versus 0 W cm^{-2}). Furthermore, when laser intensity reaches up to 1.6 W cm^{-2}, the cell viability reduces to less than 10% and negligible living cells can be detected (Figure 7a). In addition, the effects of irradiation time (0–8 min) on cell viabilities were also studied under the irradiation of 915-nm laser (1.0 W cm^{-2}; maintained ≈50 °C) (Figure 7b). With the increasing of irradiation time (such as 2 min), the cell viability goes down remarkably (such as $P < 0.01$ for 2 versus 0 min). Particularly, when the irradiation time prolongs to 8 min, cell viability decreases to less than 16% and almost no living cells are examined.

Simultaneously, to visually evaluate the photothermal therapeutic efficiency, cancer cells were stained with calcein-AM and ethidium homodimer-1 after above treatment to discern dead (red) and live (green) cells, respectively (Figure 7c,d). Noticeably, most death cells are observed when the laser intensity increases to 1.6 W cm^{-2} or irradiation time prolongs to 8 min, which agrees well with the previous cells proliferation rate

results from CCK-8 assay (Figure 7a,b). All these comparable results demonstrate the apparent and controllable tendency of photothermal therapeutic effect for cancer cells, resulting from the excellent photothermal performances of FeS$_2$-350.

### 2.4. T_2-Weighted MRI and NIR Imaging Guided Photothermal Therapy In Vivo

Based on their excellent MRI and NIR-PAT effects in vitro, FeS$_2$-350 may have great potential as novel "all-in-one" type multifunctional nanoparticle for in vivo imaging and therapy. To further evaluate its biomedical applications in vivo, the physiological saline (PBS) solution of FeS$_2$-350 (100 μL, 1 mg mL^{-1}) was injected into the tumor-bearing mice. The T_2-weighted MRI images were taken before and 1 h after the introtumorous injection (**Figure 8**a,b). The MRI images were also colored to allow easy visualization of the contrast changes. Distinctly, sharp contrast of the color is acquired at injection site, verifying that FeS$_2$-350 can act as effective T_2-weighted MRI contrast agents for tumors in vivo. All animal investigation conformed to the guide for the Care and Use of Laboratory Animals by the U.S. National Institutes of Health (NIH Publication no. 86-23, revised 1985) and performed in accordance with the protocols which are

approved by the Experimental Research Center of The First People's Hospital, Shanghai. Jiaotong University.

Simultaneously, to further evaluate the NIR imaging effect for guiding the therapy in vivo, SMMC-7721 tumors (6–7 mm) were intratumorally injected with FeS$_2$-350 solution (100 µL, 500 µg mL^{-1}) respectively. Then tumors were exposed to 915-nm laser with the power density of 1.0 W cm^{-2} for 8 min (maintaining at 50 ± 2 °C). The IR thermal camera was employed to monitor the temperature evaluation, and the images were taken at different time intervals during the laser irradiation (Figure 8c,d). For comparison, tumors injected with PBS were also investigated under the other identical conditions. Consequently, without the irradiation (0 min), the whole mice body clearly shows green or blue color (Figure 8c), and the mice keep a relatively normal physiological temperature distribution (Figure 8d). Upon the irradiation of the laser, the color is changed dramatically for PEGylated FeS$_2$+NIR group and the temperature of the injection region increases rapidly. After 5 min irradiation by NIR laser, the region injected with the PEGylated FeS$_2$-350 shows the red color and became brighter and larger, with the temperature maintaining at 50 ± 2 °C. While the region injected with PBS remains the initial color. Therefore, the PEGylated FeS$_2$-350 can be used as an effective infrared photothermal imaging agent for further guiding tumor therapy.

On account of their excellent photothermal therapy effect in vitro, we further evaluate the ablation efficacy by PEGylated FeS$_2$-350 for NIR-PAT in vivo. To estimate their immediate ablation efficacy to tumors, SMMC-7721 tumors (6–7 mm) were intratumorally injected with PEGylated FeS$_2$-350 solution (100 µL, 500 µg mL^{-1}) respectively. At 24 h post-injection, tumors were exposed to 915-nm laser with 1.0 W cm^{-2} for 10 min (maintaining at 50 ± 2 °C). After 48 h, the immediate photothermal ablation efficacy were studied by ultrasound (US) imaging (**Figure 9**a). For comparison, tumors-bearing mice injected with PBS or PEGylated FeS$_2$-350 without NIR laser irradiation treatment were also investigated under the other identical conditions. It should be emphasized that tumors from flow mode cannot visualize the bloodstream in tumors remarkably owing to the small size (Figure 9a, upper row). While for the B-mode from US images, tumors' surface can be captured and contrasted from the soft tissue (Figure 9a, middle row) in mice, but the interior cannot be sharply visualized.

Subsequently, the tumor-bearing mice from all groups were injected with the contrast agent via retro-orbital injection to further observe the inside of tumors, and then the increasing US contrast signal were imaged in vivo by US contrast-mode (Figure 9a, lower row). For mice from PBS, PBS+NIR or PEGylated FeS$_2$-350 (abbreviated to FeS$_2$-350 in Figure 9)
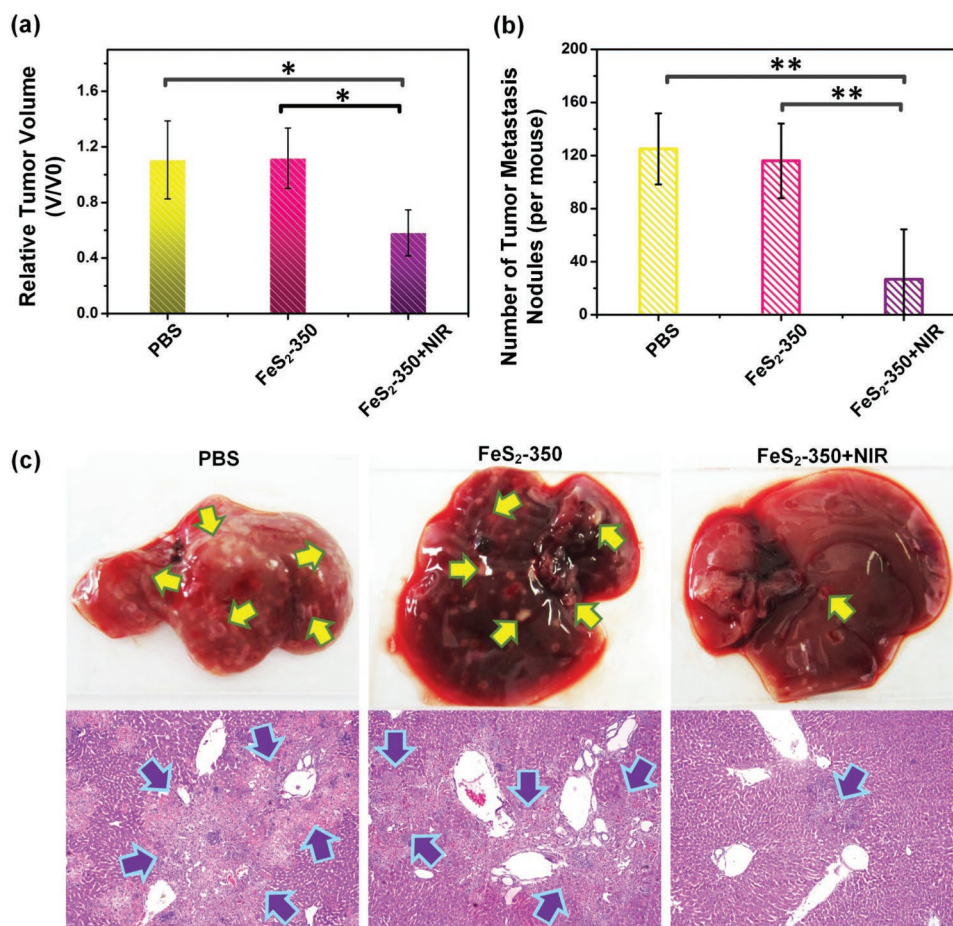
Figure 10. The short-term therapy in vivo. a) The quantification of average liver metastases tumor nodules per mouse. b) Tumor growth rate of different groups tumor-bearing mice (7 d). The size of tumors was normalized to their initial size. c) Representative liver photos and corresponding liver H&E stained slices (7 d). The magnifications are 100×. Data represent the mean ± standard deviation of six mice, *P < 0.05, **P < 0.01.

Materials
Views
www.MaterialsViews.com

ADVANCED
FUNCTIONAL
MATERIALS
www.afm-journal.de

FULL PAPER

groups, it can be clearly found that the complete power Doppler enhancement occurred immediately following slow infusion of the contrast media. Moreover one can find that the prominent color flare homogenously throughout the whole tumors suggesting negligible necrosis.[48] While, only for FeS$_2$+NIR group, the contrast agent did not completely perfuse the tumor, and it forms the black defect, potentially indicating the necrotic core within these tumors.

To further assess the above ablation efficacy, the mice were sacrificed, and tumors were collected for histological analysis, as shown in H&E stained images (Figure 9b). Noticeably, cells from groups of PBS, PBS+NIR, and PEGylated FeS$_2$-350 mostly remain their normal morphology with complete apparent membrane and nuclear structure. While after NIR laser irradiation for PEGylated FeS$_2$-350+NIR group, largest damaged areas can be distinctly observed from the image of 100× magnification (arrows), and the great majority of tumor cells are badly necrotized. Additionally, from the images of 400× magnification, cells exhibit the greatest degree of cytolysis and the loss of cell morphology. These results conform with the US imaging, further verifying that the PEGylated FeS$_2$-350 as the photothermal agent possess a remarkably immediate photothermal ablation effect for tumors.

It is well known that the most deadly aspect of cancer is its ability to metastasize, where cancer cells would like to break off from the tumor (original site) and travel to other parts of the body to generate the metastasis tumor nodules. Therefore, it is essential to inhibit the growth of metastatic tumor. For subcutaneous 7721 transplanted-tumors, cancer cells peculiarly trend to spread to the liver to generate liver metastasis. Thus, we carried out a short-term (7 d) in vivo therapy for the tumor, and estimated the number of metastasis tumor nodules in liver and monitored the tumor volume at the 7 d after treatment by injecting with PEGylated FeS$_2$-350 and then irradiating with

915-nm NIR laser (**Figure 10**). For comparison, tumors from PBS and PEGylated FeS$_2$-350 groups were also evaluated under the other identical conditions.

Remarkably, for PBS and PEGylated FeS$_2$-350 groups, tumors almost remain their initial diameter. Moreover, in livers from these two groups, a great many of off-white suspected metastasis tumor nodules are observed with dots dispersed distribution (Figure 10c arrows), and no significant difference can be found between them (Figure 10b). The suspected metastatic tumor nodules are confirmed as metastases tumor nodules according to the histopathology (H&E slices), in which mass of cells are presented with disorderly distribution in lesions and the construction of normal hepatic cords are destroyed (Figure 10c arrows). These data indicate that the growth/ metastasis of tumors could not be restrained by the materials alone without NIR laser irradiation after 7 d. While only for PEGylated FeS$_2$-350+NIR groups, the growth of tumors suffered a significant inhibition after 7 d (versus PBS or FeS$_2$-350, all $P < 0.05$, Figure 10a), and scarcely any of suspected metastases tumor nodules are acquired in this group (versus PBS or FeS$_2$-350, all $P < 0.01$, Figure 10b,c). This fact illustrates that the growth/ metastasis of tumors almost have been inhibited by photothermal effects from FeS$_2$-350 with 915-nm laser treatment. Thus, FeS$_2$-350 can be served as an effective photothermal agent not only for the photothermal therapy, but also for the inhibition of the metastases of tumors.

To cure tumors in mice, a long-term therapy of tumors was carried out for PEGylated FeS$_2$+NIR group. For comparison, mice from PEGylated FeS$_2$ group were also evaluated without laser irradiation under the same conditions (**Figure 11**). Noticeably, for FeS$_2$-350 group without laser irradiation, the volume goes up during the 24 d (Figure 11a). Quite discrepantly with FeS$_2$ groups, tumors volume in PEGylated FeS$_2$-350+NIR group
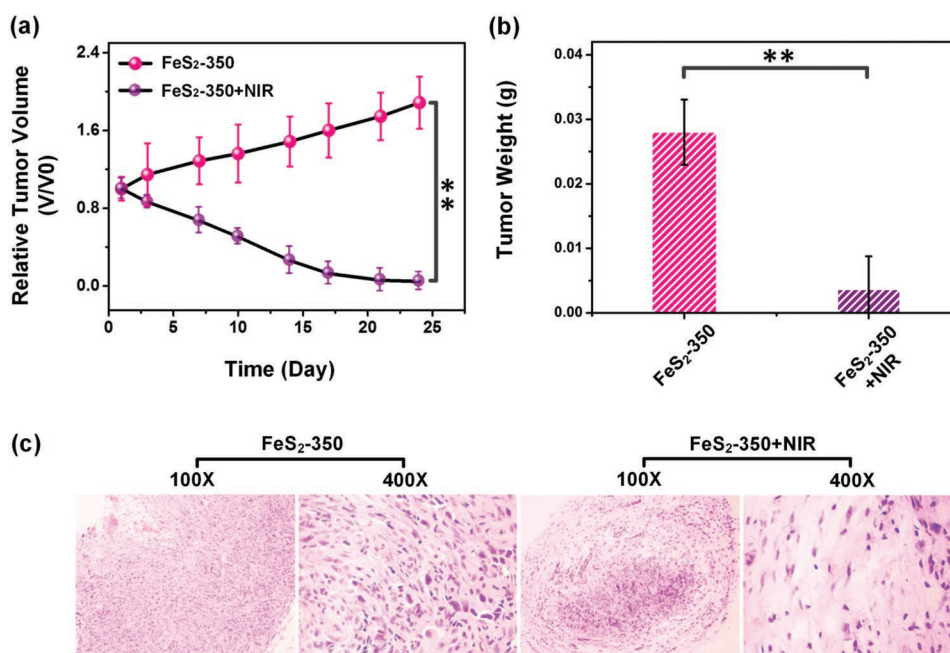
Figure 11. The long-term therapy in vivo. a) Tumor growth curves of tumor-bearing mice from different groups at 24 d post-treatments. b) Average weights of tumors. c) H&E stained tumor slices, including 100× and 400× magnifications. Data represent the mean ± standard deviation of six mice, *$P < 0.05$, **$P < 0.01$.
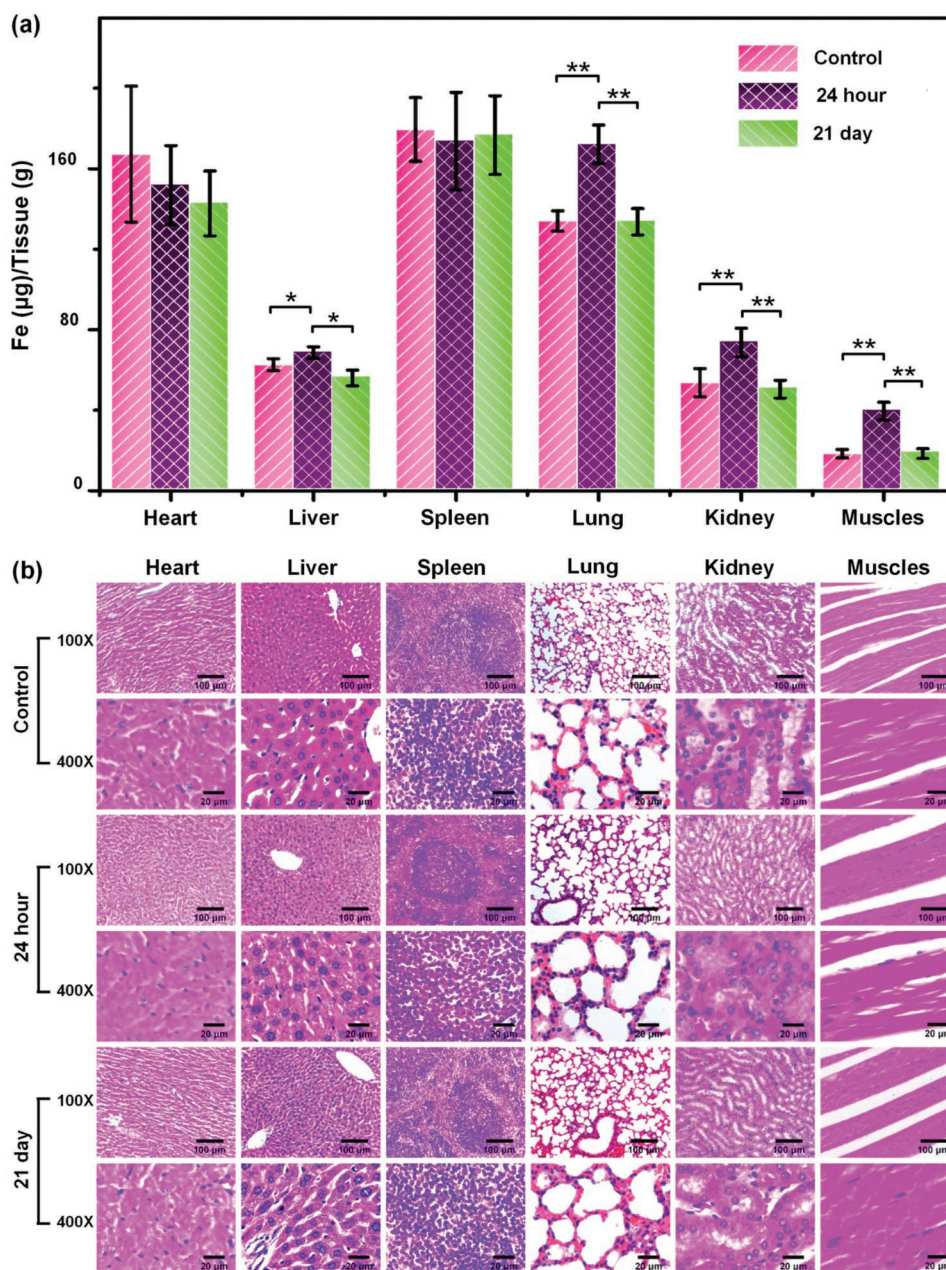
Figure 12. The biodistribution study of PEGylated FeS$_2$-350 in long-term. a) The biodistribution of PEGylated FeS$_2$-350 in various organs and tissues at different time points post-injection. b) The H&E stained slices of organs and tissues including 100× and 400× magnifications. Data represent the mean ± standard deviation of three mice, *$P < 0.05$, **$P < 0.01$.

shows continuous decrease and tends to be eliminated at 24 d post-treatments groups (versus FeS$_2$-350 $P < 0.01$). Then, mice were sacrificed at 30 d post-treatments. Tumors were collected and weighted, these results of which agree well with the tumor volume (Figure 11a,b). Eventually, the slices of the tumors were stained with hematoxylin/eosin (H&E) (Figure 11c). From the H&E stained tumor slices, FeS$_2$-350+NIR groups have suffered an aggravated fibrosis compared with FeS$_2$-350 group, in which almost cellular morphology disappears and a great number of nucleus are dissolved (with 100× and 400× magnification in Figure 11c). These results suggest that the strong photothermal

effect from FeS$_2$-350 can confer complete ablation effect for tumor.

2.5. The Toxicology Evaluation of PEGylated FeS$_2$-350 In Vivo

Finally, to further estimate the long-term biosafety of FeS$_2$-350, we carried out the biodistribution study and toxicology measurements after 24 h and 21 d post-injection (**Figure 12** and Figure S7, Supporting Information). The solutions of FeS$_2$-350 (100 µL, 1 mg mL^{-1}) were injected into leg muscles of mouse

(as an organ, $n = 9$), respectively. It should be noticed that mice without any injections were used as the control. At 24 h and 21 d post-injection, organs, tissues, and blood from mice were collected. For the biodistribution examination, organs and tissues were dissolved by aqua regia respectively. The concentration of iron from FeS_2-350 in these organs and tissues was conducted by the inductively coupled plasma atomic emission spectroscopy.

Noticeably, at 24 h post-injection, the content of iron increases remarkably in liver, lung, and kidney (versus control all $P < 0.05$, Figure 12a), and most of PEGylated FeS_2-350 is still concentrated in muscles with a higher iron content (versus control all $P < 0.05$). While, after 21 d, the content of iron in these organs deceased distinctively (versus 24 h all $P < 0.05$), tending to be in normal levels (versus control all $P > 0.05$). More importantly, the iron content in muscles also has a significant reduction and close to the untreated mice (versus control all $P > 0.05$). Therefore, one can deem that the PEGylated FeS_2-350 can be excreted from the mice body. Meanwhile, from the obtained H&E staining of tumor slices at 24 h or 21 d (Figure 12b), we find that there is no necrosis or apoptosis in cells, or any damages in organs or tissues such as in heart, liver, spleen, lung, kidney, and mussels, demonstrating the long-term biosafety of the PEGylated FeS_2-350. In addition, the liver function indicators and parameters from the routine text of blood are all close to those of control group and belong to the normal reference ranges (Figure S7, Supporting Information),[49] verifying lower toxicity and no side effects of PEGylated FeS_2-350 to mice.

3. Conclusion

In summary, we have successfully prepared "all-in-one" type multifunctional FeS_2-350 nanoparticles. One FeS_2-350 nanoparticle has all required properties for the diagnosis and therapy of tumor, including the increased photoabsorption in visible-NIR region and then strong NIR photothermal effect, excellent magnetic property and low cytotoxicity. When the PBS dispersion of FeS_2-350 nanoparticle is injected into the tumor of mice, tumor can be detected simultaneously by MRI and NIR dual-modal imaging. Furthermore, due to the photothermal effect of FeS_2-350, cancer cells in vivo can be efficiently destroyed, the tumor tends to be eliminated, and the tumor metastasis has been inhibited. Therefore, the present FeS_2-350 nanoparticles can be served as a promising theranostic nanoplatform for dual MRI/NIR-thermal imaging guided photothermal therapy of tumor. More importantly, this work provides some insight into the design and development of other "all-in-one" type of multifunctional nanoparticle with single component for the imaging guided therapy of tumor.

Supporting Information

Supporting Information is available from the Wiley Online Library or from the author.

Acknowledgements

[1] D. E. Lee, H. Koo, I. C. Sun, J. H. Ryu, K. Kim, I. C. Kwon, *Chem. Soc. Rev.* **2012**, *41*, 2656.

[2] a) L. S. Lin, Z. X. Cong, J. B. Cao, K. M. Ke, Q. L. Peng, J. Gao, H. H. Yang, G. Liu, X. Chen, *ACS Nano* **2014**, *8*, 3876; b) C. Zhang, W. Bu, D. Ni, S. Zhang, Q. Li, Z. Yao, J. Zhang, H. Yao, Z. Wang, J. Shi, *Angew. Chem. Int. Ed.* **2016**, *55*, 2101.

[3] X. Liang, Y. Li, X. Li, L. Jing, Z. Deng, X. Yue, C. Li, Z. Dai, *Adv. Funct. Mater.* **2015**, *25*, 1451.

[4] a) T. D. MacDonald, T. W. Liu, G. Zheng, *Angew. Chem.* **2014**, *126*, 7076; b) E. M. Gale, I. P. Atanasova, F. Blasi, I. Ay, P. Caravan, *J. Am. Chem. Soc.* **2015**, *137*, 15548.

[5] J. Zhou, Q. Liu, W. Feng, Y. Sun, F. Li, *Chem. Rev.* **2015**, *115*, 395.

[6] G. Hong, S. Diao, A. L. Antaris, H. Dai, *Chem. Rev.* **2015**, *115*, 10816.

[7] N. Lee, S. H. Choi, T. Hyeon, *Adv. Mater.* **2013**, *25*, 2641.

[8] W. Eck, A. I. Nicholson, H. Zentgraf, W. Semmler, S. Bartling, *Nano Lett.* **2010**, *10*, 2318.

[9] B. Li, K. Ye, Y. Zhang, J. Qin, R. Zou, K. Xu, X. Huang, Z. Xiao, W. Zhang, X. Lu, *Adv. Mater.* **2015**, *27*, 1339.

[10] M. Wu, Q. Meng, Y. Chen, Y. Du, L. Zhang, Y. Li, L. Zhang, J. Shi, *Adv. Mater.* **2015**, *27*, 215.

[11] Z. Meng, F. Wei, R. Wang, M. Xia, Z. Chen, H. Wang, M. Zhu, *Adv. Mater.* **2016**, *28*, 245.

[12] a) S. S. Lucky, K. C. Soo, Y. Zhang, *Chem. Rev.* **2015**, *115*, 1990; b) L. Cheng, C. Wang, L. Feng, K. Yang, Z. Liu, *Chem. Rev.* **2014**, *114*, 10869.

[13] X. Zhu, W. Feng, J. Chang, Y. W. Tan, J. Li, M. Chen, Y. Sun, F. Li, *Nat. Commun.* **2016**, *7*. 10437

[14] Z. Sheng, D. Hu, M. Zheng, P. Zhao, H. Liu, D. Gao, P. Gong, G. Gao, P. Zhang, Y. Ma, L. Cai, *ACS Nano* **2014**, *8*, 12310.

[15] a) M. S. Yavuz, Y. Cheng, J. Chen, C. M. Cobley, Q. Zhang, M. Rycenga, J. Xie, C. Kim, K. H. Song, A. G. Schwartz, L. V. Wang, Y. Xia, *Nat. Mater.* **2009**, *8*, 935; b) W. Wu, J. Shen, P. Banerjee, S. Zhou, *Biomaterials* **2010**, *31*, 7555.

[16] a) Q. Tian, M. Tang, Y. Sun, R. Zou, Z. Chen, M. Zhu, S. Yang, J. Wang, J. Wang, J. Hu, *Adv. Mater.* **2011**, *23*, 3542; b) Z. Chen, Q. Wang, H. Wang, L. Zhang, G. Song, L. Song, J. Hu, H. Wang, J. Liu, M. Zhu, D. Zhao, *Adv. Mater.* **2013**, *25*, 2095.

[17] Q. Tian, F. Jiang, R. Zou, Q. Liu, Z. Chen, M. Zhu, S. Yang, J. Wang, J. Wang, J. Hu, *ACS Nano* **2011**, *5*, 9761.

[18] W. Xu, Q. Tian, Z. Chen, M. Xia, D. K. Macharia, B. Sun, L. Tian, Y. Wang, M. Zhu, *J. Mater. Chem. B* **2014**, *2*, 5594.

[19] Q. Chen, C. Wang, Z. Zhan, W. He, Z. Cheng, Y. Li, Z. Liu, *Biomaterials* **2014**, *35*, 8206.

[20] C. Tian, L. Zhu, F. Lin, S. G. Boyes, *ACS Appl. Mater. Interfaces* **2015**, *7*, 17765.

[21] H. Gong, Z. Dong, Y. Liu, S. Yin, L. Cheng, W. Xi, J. Xiang, K. Liu, Y. Li, Z. Liu, *Adv. Funct. Mater.* **2014**, *24*, 6492.

[22] X. Liu, I. Marangon, G. Melinte, C. Wilhelm, C. Ménard Moyon, B. P. Pichon, O. Ersen, K. Aubertin, W. Baaziz, C. Pham Huu, S. Bégin Colin, A. Bianco, F. Gazeau, D. Bégin, *ACS Nano* **2014**, *8*, 11290.

[23] Y. Lu, C. Shi, M. J. Hu, Y. J. Xu, L. Yu, L. P. Wen, Y. Zhao, W. P. Xu, S. H. Yu, *Adv. Funct. Mater.* **2010**, *20*, 3701.

[24] L. Landgraf, C. Christner, W. Storck, I. Schick, I. Krumbein, H. Dähring, K. Haedicke, K. Heinz-Herrmann, U. Teichgräber, J. R. Reichenbach, W. Tremel, S. Tenzer, I. Hilger, *Biomaterials* **2015**, *68*, 77.

[25] X. D. Zhang, J. Chen, Y. Min, G. B. Park, X. Shen, S. S. Song, Y. M. Sun, H. Wang, W. Long, J. Xie, K. Gao, L. Zhang, S. Fan, F. Fan, U. Jeong, *Adv. Funct. Mater.* **2014**, *24*, 1718.

[26] a) Z. C. Wu, W. P. Li, C. H. Luo, C. H. Su, C. S. Yeh, *Adv. Funct. Mater.* **2015**, *25*, 6527; b) Q. Tian, J. Hu, Y. Zhu, R. Zou, Z. Chen, S. Yang, R. Li, Q. Su, Y. Han, X. Liu, *J. Am. Chem. Soc.* **2013**, *135*, 8571.

[27] R. Lv, P. Yang, F. He, S. Gai, C. Li, Y. Dai, G. Yang, J. Lin, *ACS Nano* **2015**, *9*, 1630.

[28] L. Cheng, J. Liu, X. Gu, H. Gong, X. Shi, T. Liu, C. Wang, X. Wang, G. Liu, H. Xing, *Adv. Mater.* **2014**, *26*, 1886.

[29] G. Tian, X. Zhang, X. Zheng, W. Yin, L. Ruan, X. Liu, L. Zhou, L. Yan, S. Li, Z. Gu, Y. Zhao, *Small* **2014**, *10*, 4160.

[30] B. Li, K. Ye, Y. Zhang, J. Qin, R. Zou, K. Xu, X. Huang, Z. Xiao, W. Zhang, X. Lu, J. Hu, *Adv. Mater.* **2015**, *27*, 1339.

[31] T. Fu, Y. Chen, J. Hao, X. Wang, G. Liu, Y. Li, Z. Liu, L. Cheng, *Nanoscale* **2015**, *7*, 20757.

[32] K. Yang, G. Yang, L. Chen, L. Cheng, L. Wang, C. Ge, Z. Liu, *Biomaterials* **2015**, *38*, 1.

[33] J. M. Luther, P. K. Jain, T. Ewers, A. P. Alivisatos, *Nat. Mater.* **2011**, *10*, 361.

[34] G. Xi, S. Ouyang, P. Li, J. Ye, Q. Ma, N. Su, H. Bai, C. Wang, *Angew. Chem. Int. Ed.* **2012**, *51*, 2395.

[35] a) A. Kirkeminde, R. Scott, S. Ren, *Nanoscale* **2012**, *4*, 7649; b) H. A. Macpherson, C. R. Stoldt, *ACS Nano* **2012**, *6*, 8940.

[36] P. Xiao, X. L. Fan, L.-M. Liu, W. M. Lau, *Phys. Chem. Chem. Phys.* **2014**, *16*, 24466.

[37] J. Puthussery, S. Seefeld, N. Berry, M. Gibbs, M. Law, *J. Am. Chem. Soc.* **2011**, *133*, 716.

[38] a) B. Yuan, W. Luan, S. T. Tu, *Dalton Trans.* **2012**, *41*, 772; b) D. Wang, Q. Wang, T. Wang, *CrystEngComm* **2010**, *12*, 3797.

[39] J. Puthussery, S. Seefeld, N. Berry, M. Gibbs, M. Law, *J. Am. Chem. Soc.* **2010**, *133*, 716.

[40] D. W. Wang, Q. H. Wang, T. M. Wang, *CrystEngComm* **2010**, *12*, 755.

[41] a) L. Yu, S. Lany, R. Kykyneshi, V. Jieratum, R. Ravichandran, B. Pelatt, E. Altschul, H. A. S. Platt, J. F. Wager, D. A. Keszler, A. Zunger, *Adv. Energy Mater.* **2011**, *1*, 748; b) F. Herbert, A. Krishnamoorthy, W. Ma, K. Van Vliet, B. Yildiz, *Electrochim. Acta* **2014**, *127*, 416.

[42] J. Hu, Y. Zhang, M. Law, R. Wu, *Phys. Rev. B* **2012**, *85*, 085203.

[43] R. Morrish, R. Silverstein, C. A. Wolden, *J. Am. Chem. Soc.* **2012**, *134*, 17854.

[44] M. Wang, C. Xing, K. Cao, L. Zhang, J. Liu, L. Meng, *J. Mater. Chem. A* **2014**, *2*, 9496.

[45] X. Liu, X. Wang, B. Zhou, W. C. Law, A. N. Cartwright, M. T. Swihart, *Adv. Funct. Mater.* **2013**, *23*, 1256.

[46] a) Z. C. Wu, W. P. Li, C. H. Luo, C. H. Su, C. S. Yeh, *Adv. Funct. Mater.* **2015**, *25*, 6527; b) L. H. Reddy, J. L. Arias, J. Nicolas, P. Couvreur, *Chem. Rev.* **2012**, *112*, 5818.

[47] L. Zeng, W. Ren, L. Xiang, J. Zheng, B. Chen, A. Wu, *Nanoscale* **2013**, *5*, 2107.

[48] Z. Xing, J. Wang, H. Ke, B. Zhao, X. Yue, Z. Dai, J. Liu, *Nanotechnology* **2010**, *21*, 145607.

[49] Research Animal Models Charles River, http://www.criver.com/en-US/ProdServ/ByType/ResModOver/ResMod/Pages/BALBc-Mouse.aspx; (accessed August 2016).